Published in final edited form as:

J Am Chem Soc. 2019 February 27; 141(8): 3641–3653. doi:10.1021/jacs.8b13134.

A Nonheme Thiolate-ligated Cobalt Superoxo Complex: Synthesis and Spectroscopic Characterization, Computational Studies, and Hydrogen Atom Abstraction Reactivity

Jesse B. Gordon[a], **Avery C. Vilbert**[b], **Maxime A. Siegler**[a], **Kyle M. Lancaster**[b], **Pierre Moënne-Loccoz**[c], and **David P. Goldberg**[*,a]

[a]Department of Chemistry, The Johns Hopkins University, 3400 North Charles Street, Baltimore, Maryland 21218, United States

[b]Department of Chemistry and Chemical Biology, Baker Laboratory, Cornell University, Ithaca, NY 14853, United States

[c]Department of Biochemistry & Molecular Biology, Oregon Health & Science University, Portland, Oregon 97239-3098, United States

Abstract

The synthesis and characterization of a Co(II) dithiolato complex Co(M_{e3}TACN)(S_2SiMe_2) (**1**) is reported. Reaction of **1** with O_2 generates a rare thiolate-ligated cobalt-superoxo species Co(O_2)(M_{e3}TACN)(S_2SiMe_2) (**2**) that was characterized spectroscopically and structurally by resonance Raman, EPR, and X-ray absorption spectroscopies as well as density functional theory (DFT). Metal-superoxo species are proposed to S-oxygenate metal-bound thiolate donors in nonheme thiol dioxygenases, but **2** does not lead to S-oxygenation of the intramolecular thiolate donors, and does not react with exogenous sulfur donors. However, complex **2** is capable of oxidizing the O-H bonds of 2,2,6,6-tetramethylpiperidin-1-ol (TEMPOH) derivatives via H-atom abstraction. Complementary proton-coupled electron-transfer (PCET) reactivity is seen for **2** with separated proton/reductant pairs. The reactivity studies indicate that **2** can abstract H-atoms from weak X-H bonds with BDFE ≤70 kcal mol-1. DFT calculations predict that the putative Co(OOH) product has an O-H bond dissociation free energy (BDFE) = 67 kcal mol^{-1}, which matches the observed pattern of reactivity seen for **2**. These data provide new information regarding the selectivity of S-oxygenation versus H-atom abstraction in thiolate-ligated nonheme metalloenzymes that react with O_2.

Graphical Abstract

[*]**Corresponding Authors:** dpg@ihu.edu, kml236@cornell.edu, moennelo@ohsu.edu.

Supporting Information

The Supporting Information is available free of charge on the ACS Publications website.

^{1}H NMR, ^{2}H NMR, and UV-vis spectra, cyclic voltammetry data, EXAFS data, metrical parameters for DFT-computed structures, DFT conformer energy calculations, DFT-derived MO diagrams, TEMPO EPR calibration data, kinetics data, and crystallo-graphic information for **1** (PDF)

The authors declare no competing financial interests

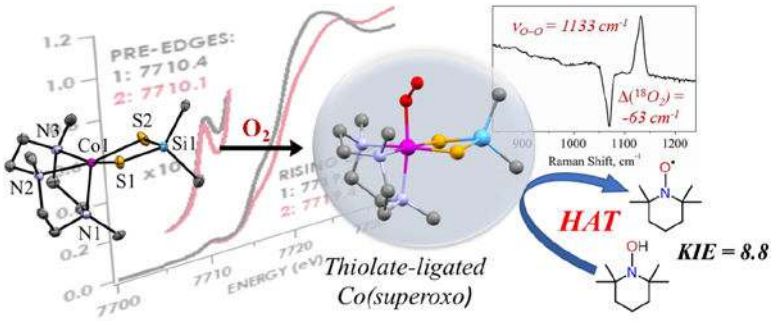

Introduction

The activation of dioxygen is of fundamental importance to a number of synthetic and biological transformations.[1] The metal-mediated binding and concomitant one-electron reduction of O_2 to generate a metal-superoxido species is implicated as the first key step in substrate oxidation reactions in biology,[2] catalysis,[3–4] and the oxygen reduction reaction (ORR).[5] Determining the influence of ligand architecture and donor type, as well as metal ion identity, oxidation and spin states, on the binding and activation of O_2 continues to be a focus of much research.

The activation of O_2 and its reduced analogues (e.g. O_2•–, H_2O_2) by sulfur-ligated iron centers is of special importance to certain nonheme iron enzymes, including thiol dioxygenases, isopenicillin N synthase (IPNS), superoxide reductase, persulfide dioxygenase (ETHE1), and the sulfoxide synthases, EgtB and OvoA. Proposed mechanisms for these enzymes invoke the formation of Fe^{III}-superoxo ($Fe^{III}(O_2$•–)) intermediates, which are believed to be responsible for oxidation reactions, such as hydrogen-atom abstraction or S-oxygenation.

In the case of IPNS, experimental evidence supports a mechanism in which the first H-atom transfer (HAT) step in the cyclization of the tripeptide substrate δ-(L-α-aminoadipoyl)-L-cysteinyl-D-valine (ACV) is mediated by an $Fe^{III}(O_2$•–) species.[6] In cysteine dioxygenase (CDO), a mammalian thiol dioxygenase, an $Fe^{III}(O_2$•–) intermediate is proposed to selectively attack the metal-bound thiolate, initiating the dioxygenation of cysteine to cysteine sulfinic acid, despite the presence of a nearby cysteine-crosslinked tyrosine residue that should be susceptible to H-atom abstraction (Figure 1).[7–9]

The sulfoxide synthases EgtB and OvoA catalyze C-S bond formation between cysteine- and histidine-derived residues as well as S-oxygenation, to give a final coupled sulfoxide product. However, the mechanism, and especially the ordering of S-oxygenation versus C-S bond insertion for either of these enzymes, is unknown. One proposed mechanism involves initial sulfur attack by $Fe^{III}(O_2$•–) to form an Fe^{IV}(O)(sulfenate) intermediate, similar to what has been suggested for CDO, followed by eventual insertion of the sulfenate into the His C-H bond. Alternatively, the $Fe^{III}(O_2$•–) in termediate may first abstract hydrogen from a tyrosine residue in close proximity to the Fe center, generating Fe^{III}(OOH) and a tyrosyl radical (Figure 1).[10–11] A series of subsequent steps leads to C-S bond formation and sulfoxidation of the thioether to give the final product. The EgtB mutant $EgtB_{Y377F}$, which

replaces the proximal tyrosine with a phenylalanine group, no longer performs the C-S insertion reaction, and instead performs CDO-like S-oxygenation reactivity.[12] Furthermore, studies with OvoA indicate that mutation of the proximal Tyr group can modulate the amount of sulfinate versus sulfoxide products observed.[10] These studies suggest that the Tyr plays a key role in the reactivity of the sulfoxide synthases, and perhaps H-atom transfer from Tyr biases the outcome toward C-S bond formation versus S-oxygenation. It is not yet understood what features of thiolate-ligated $M(O_2^{\bullet-})$ species favor S-oxygenation versus H-atom abstraction.

Early work on the oxidative reactivity of synthetic metal-superoxo species with organic substrates highlighted the ability of Co complexes to catalyze the oxidation of substituted phenols in the presence of dioxygen. These studies implicated H-atom abstraction by a Co-superoxo intermediate as the key step that initiates phenol oxidation.[13–21] However, the latter studies often involved observations made under catalytic conditions, and did not examine well-characterized $Co(O_2^{\bullet-})$ species in direct reaction with H-atom donors. Recently, the isolated H-atom abstraction step has been studied in detail with well-defined iron and cobalt superoxo species.[22–26] Iron and cobalt superoxo complexes have been shown to exhibit both electrophilic and nucleophilic reactivity,[26–27] including a recent case of a Co^{II}(superoxo)($L^{\bullet}$) species formed via leveraging ligand aminyl/amide redox chemistry. This species was shown to mediate catalytic O-atom transfer to phosphines as well as catalytic aldehyde deformylation.[27]

Nonheme metal superoxo species bearing thiolate donors remain exceedingly rare, with only two well-characterized examples (Co and Fe),[28–29] and in these cases, no substrate reactivity studies were reported. Thiolate coordination is likely to strongly influence the reactivity properties of these species. Late transition metal-thiolate bonds are characterized by high covalency. The archetypal example is the bonding of oxidized blue copper centers, where the redox-active singly occupied molecular orbital is of effectively equal Cu 3d and S 3p parentage, facilitating rapid electron transfer.[30] Co-S covalency could in principle afford another means toward generation of a Co-superoxo while effectively foregoing Co-centered redox in a manner analogous to the aforementioned Co^{II}(superoxo)($L^{\bullet}$).

To investigate the bonding and reactivity of a thiolate-supported Co-superoxo species, we prepared a novel dithiolate-li-gated cobalt(II) complex, $Co^{II}(M_{e3}TACN)(S_2SiM_{e2})$ (**1**). We show that reaction of **1** with O_2 leads to the mononuclear cobalt superoxo complex $Co(O_2)(M_{e3}TACN)(S_2SiM_{e2})$ (**2**), which was characterized structurally by X-ray absorption spectroscopy (XAS), and spectroscopically by electron paramagnetic resonance (EPR) and resonance Raman (RR) spectroscopies. Density functional theory (DFT) calculations were performed to support the spectroscopic analyses. The spectroscopic and calculational results best accord with the view that superoxide formation occurs via redox reactivity best described as $[CoS_2]^{0/1+}$ rather than $Co^{2+/3+}$. Treatment of **1** with O_2 to form superoxide is attended by an increase in the degree of Co-S mixing in unoccupied molecular orbitals, allowing the Co to remain in the +2 oxidation state in both species. We then show that while **2** does not oxygenate the sulfur ligands or exogenous sulfur substrates, it is capable of H-atom abstraction reactivity with weak O-H bonds.

Results and Discussion

Synthesis.

Compound **1** was prepared by mixing Me3TACN and $Co(OAc)_2$ in an equimolar ratio in THF followed by heating to 60 °C, resulting in a purple solution. Following cooling of the solution to 24 °C, addition of 1 equiv of hexamethylcyclotrisilathiane ($(Me_2SiS)_3$) in hexane caused an immediate color change to green, and eventual formation of a blue-green precipitate.

Isolation of the blue-green solid followed by recrystallization from vapor diffusion of pentane into a THF solution of crude **1** results in the formation of blue-green crystals over 48 h (52%). The single crystal X-ray diffraction analysis (XRD) reveals that **1** is a five-coordinate Co^{II} complex with a tau value[31] = 0.107, indicating a square pyramidal geometry. This structure is similar to the analogous Fe^{II} complex previously described.[32] The Co-S distances differ by 0.043 Å, and these distances, and the Co-N average distance (2.19 Å), show minor bond contractions compared to the Fe^{II} an alogue, as expected for the smaller ionic radius for Co^{II}.[33–35] The ^1H NMR spectrum of **1** in CD_3CN is consistent with a high-spin Co^{II} center, exhibiting paramagnetically shifted resonances from −55 to 100 ppm. Assignment of the N-Me peak was made possible by synthesis of the selectively deuterated **1-*d*$_9$**. A peak at −52.5 ppm is absent in the ^1H NMR spectrum of **1-*d*$_9$** (Figure S1), and the corresponding ^2H NMR spectrum reveals a single peak at −53 ppm. These data allow us to assign the latter peaks to the N-Me protons, which appear magnetically equivalent in solution. The ^1H NMR spectrum for **1** is similar in CD_3CN and THF-d_8, suggesting that solvent does not coordinate to the open site (Figure S2). The solution magnetic moment of **1** was measured by Evans method, giving μ_{eff} = 4.89 μ_B, which is significantly higher than the expected spin-only value, but is typical for Co^{II} (S = 3/2) complexes with significant orbital angular momentum.[36–39]

The X-band EPR spectrum of **1** in a butyronitrile glass at 12 K is shown in Figure 2b, and is consistent with a S = 3/2 system, with g = 6.1, 3.5, 2.7. Cyclic voltammetry of **1** reveals a single quasi-reversible wave ($E_{1/2}$ = −0.81 V vs. Fc^+/Fc; ΔE_{pp} = 200 mV) (Figure 2c). The Co^{II} center in **1** is thus highly reducing compared to other Co^{II} complexes that bind O_2,[22,25,28,40] likely because of the strongly donating, dianionic dithiolato ligand set.

Dioxygen Reactivity.

Addition of O_2 to a solution of **1** in 2-methyltetrahydrofuran (2-MeTHF), THF, dichloromethane, or butyronitrile at −80 °C results in an immediate color change from pale purple to orange. UV-visible spectroscopy shows the appearance of an intense band at 340 nm (ε = 12600 M^{-1} cm^{-1}) and a shoulder at 360 nm (ε =10600 M^{-1} cm^{-1}), as well as bands at 445 (ε = 3100 M^{-1} cm^{-1}) and 555 nm (ε = 1300 M^{-1} cm^{-1}) corresponding to a new species 2 (Figure 3). This species is stable indefinitely at −80 °C. Titration of an O_2-saturated solution of 2-MeTHF at −135 °C into **1** confirms the 1:1 Co/O_2 stoichiometry for the formation of **2** (Figure S5), consistent with the formation of a mononuclear Co/O_2 species. Bubbling argon for one hour through a solution of **2** results in no spectral change,

and the formation of **2** cannot be reversed by repeated vacuum/purge cycles. Thus, the binding of O_2 to **1** is irreversible.

The resonance Raman spectrum of **2** obtained in frozen 2-MeTHF with λ_{exc} = 407 nm exhibits a peak at 1133 cm^{-1}, which shifts to 1070 cm^{-1} upon $^{18}O_2$ substitution. This down-shift of 63 cm^{-1} is comparable to the expected shift of 65 cm^{-1} predicted by Hooke's law for an O-O bond. This ν(O-O) frequency is within the typical range seen for six-coordinate, end-on, Co-superoxo complexes.[45] Another O_2-sensitive band at 1123 cm^{-1} ($\Delta\nu(^{18}O_2 - ^{16}O_2) = -64$ cm^{-1}) suggests the presence of a second superoxo conformer; these two ν(O-O) components likely reflect different rotamers of the superoxo ligand relative to the N2S2 equatorial plane. A DFT geometry scan varying the N-Co-O-O dihedral angle shows a relatively flat potential energy surface, supporting the assignment of the two ν(O-O) components (vide infra). The presence of two conformations for Co-superoxo species has also been suggested from RR data for oxycobalt hemoglobin[44] and a corrole Co-superoxo complex.[43] In the latter complex, two O-O stretches were observed, resulting from either two conformers or the presence of Fermi coupling. In the case of **2**, Fermi coupling is ruled out by the fact that $^{18}O_2$ substitution results in no change in the relative intensity of the two observed vibrational bands. The O-O stretching frequencies in **2** are on the low end of the range reported for other 6-coordinate Co-superoxo complexes (Table 1), likely due to the presence of the strongly donating thiolate ligands in **2**. Additional O_2-sensitive RR bands are seen for **2** at 520 cm^{-1} ($\Delta\nu(^{18}O_2 - ^{16}O_2) = -29$ cm^{-1}) and 367 cm^{-1} ($\Delta\nu(^{18}O_2 - ^{16}O_2) = -9$ cm^{-1}). These bands are assigned to the Co-O stretching and Co-O_2 bending modes, respectively, which is supported by density functional theory (DFT) calculations (vide infra). A Badger's rule analysis[46] of the O-O stretch at 1133 cm^{-1} predicts an O-O bond length of 1.34 Å, which matches the bond length obtained from DFT calculations (vide infra).

The X-band EPR spectrum of **2** in 2-MeTHF obtained at 12 K exhibits a rhombic signal with g ~2.11, 2.02, and 1.98 from simulation of the experimental spectrum. Simulating the spectrum with a single species gave unsatisfactory results. However, an improved simulation required a second species with g ~2.11, 2.03, and 2.02, representing ~30% of the signal. The requirement of two species for a good EPR simulation is consistent with the resonance Raman data that indicates two conformers exist in a similar ratio to that seen by EPR. Resolved Co hyperfine splitting showing 8 lines is observed on the high g side of the spectrum with hyperfine coupling constant $A(^{59}Co) = 30.3$ G for the major species. The significantly smaller cobalt hyperfine coupling constant for **2** as compared to **1** is consistent with the un-paired electron residing primarily on the superoxido ligand. These spectral features are typical for a mononuclear Cosuperoxo species.[28, 47–49]

Co K-edge X-ray absorption spectroscopy (XAS) was carried out to evaluate the participation of Co in the redox reaction between **1** and O_2. Differences in the spectra of **1** and **2** are predominantly absorptivity-based, and rising edge energies vary insignificantly. The pre-edge region of the K-edge XAS spectrum obtained for **1** shows a clearly resolved peak at 7710.4 eV, and the rising edge inflection point occurs at 7719.5 eV. The spectrum obtained for **2** itself shows a distinct pre-edge peak, although this peak is red-shifted by 0.3 eV to 7710.1 eV. The rising edge of the spectrum obtained for **2** appears at 7719.4 eV. While rising edge energies are commonly used to ascertain differences in physical oxidation state,

we and others have noted that changes to coordination geometry and ligand identity can confound these interpretations.[50–51] In the current case, addition of a sixth ligand to **1** results in diminished intensity, but no significant edge shifts. Addition of electronegative donors such as O would be expected to lead to a blue shift of the rising edge even in the absence of Co-centered redox. That the energies remain invariant suggest that not only does the Co not undergo oxidation, but that the metal center may have obtained a higher electron population.

Changes to the structural and electronic properties at Co upon formation of **2** are more clearly evident following analysis of the extended X-ray absorption fine structure (EXAFS) in the Co K-edge XAS. The EXAFS of **1** is in good agreement with the XRD data, providing best fits with Co-N_{ave} = 2.14 Å and Co-S_{ave} = 2.36 Å. The EXAFS of **2** is best fit with a 6-coordinate Co ion, including three Co-N/O scatterers at 2.04 Å, two Co-S_{ave} = 2.29 Å, and one short Co-N/O scatterer at 1.85 Å. The Co-N/O scatterer at 1.85 Å is assigned to the Co-O_2 bond, which is in agreement with a 1.90 Å distance predicted from a Badger's rule analysis using the experimental vibrational data. The contractions in Co-N and Co-S bond distances in **2** are consistent with a change from an $S = 3/2$, hs-Co^{II} center in **1** to an $S = 1/2$ species upon binding O_2. Shortening of the Co-S distances would also lead to a greater degree of Co 3d/S 3p mixing, which would de-localize hole character from Co to S.

Geometry optimization of **1** by DFT accurately reproduced the metrical parameters for this complex as determined by XRD. The DFT geometry optimization for **2** produces a 6-coordinate Co center that is bound by one oxygen atom, two sulfur and three nitrogen atoms, and exhibits bond metrics that reproduce the EXAFS data (Table S4). The resonance Raman spectra indicated that there are likely two Co($O_2^{\bullet-}$) conformers, and a DFT geometry scan of different orientations of the $O_2^{\bullet-}$ ligand along the N2S2 equatorial plane reveals that different conformers are close in energy, with barriers to rotation < 2 kcal mol^{-1}(Figure S8). Due to the inherent errors in calculating energies by DFT,[52] it is not possible to definitively assign which two rotamers are present in solution. However, frequency calculations on several of these rotamers reveals that the O-O stretching frequency varies by as much as 15 cm^{-1}, consistent with the experimental vibrational data, which shows a shift of 10 cm^{-1} for the two conformations. Taken together, the DFT data support the presence of two conformers of **2** present in solution. All subsequent calculations utilize the conformer **2-A**, which most closely matches the experimental data for the major conformer (see Supporting Information). Frequency calculations predict an O-O stretching frequency of 1126 cm^{-1}, a Co-O stretching frequency of 518 cm^{-1} and a Co-O_2 bending mode at 363 cm^{-1}, which match closely with the experimental data. The calculated O-O bond length is 1.311 Å, which is close to that calculated by Badger's rule using the experimental vibrational data and consistent with the superoxido character of the O_2 unit.

The electronic structures of **1** and **2** were calculated by DFT to provide further insight into the experimental data. An electronic configuration of $\left[d_{xz}^2, d_{xy}^2, d_{yz}^1, d_{z^2}^1, d_{x^2-y^2}^1\right]$ for **1** was calculated, with predominantly sulfur character in the Co-S **π**-bonding orbitals, and mainly Co character in the corresponding S-Co **π*** orbitals. In contrast, the **π*** anti-bonding orbitals in **2** are predominantly S in character, suggesting a large degree of covalency within

the complex. This covalency also likely contributes to a donation of electron density into the O_2 π* orbitals, which in turn should weaken the O-O bond in comparison to non-thiolate-ligated Co-superoxo complexes. The singly occupied molecular orbital is primarily O_2 π*op in character (where op is out of plane with respect to the Co-O-O plane). Löwdin spin population analysis reveals that a significant amount of spin density is localized on the $O_2^{\bullet-}$ ligand, with a small amount remaining on the cobalt center (O_2: 93.4%; Co: 3.1%), corroborating the EPR data.

As predicted by the EXAFS structural analysis, a substantial elevation of Co-S covalency attends oxygenation of **1**. The two LUMOs of **2** feature substantially lower Co 3d character than the three SOMOs of **1** (Figure 6). Weighting the four vacancies among the two LUMOs of **2** by their Co 3d character, it is estimated that **2** is lacking 2.3 electrons from the Co 3d manifold. Taking a similar approach to **1**, there are 2.6 holes in the d-manifold. This observation suggests that $[CoS_2]^{0/1+}$ is the redox couple that should be invoked in reactivity with O_2. Moreover, the apparent *increase* in d-count on going from **1** to **2** accords with the observed XAS behaviour. Taken together, the DFT calculations provide good support for the structural and spectroscopic data obtained for **2**.

Substrate Reactivity.

Thiolate ligands can be susceptible to oxidation, e.g. through S-oxygenation or disulfide formation by reaction with O_2.[53–59] However, complex **2** exhibits good stability at low temperature, indicating that there is no direct attack of O_2 on the S donors under these conditions. Complex **2** also appears unreactive toward external reductants such as PPh3, PhSMe, PhSH, or cysteine methyl ester. However, **2** does react with the hydrogen atom donors 4-methoxy−2,2,6,6-tetramethylpiperidin−1-ol (4-OMe-TEMPOH) and 2,2,6,6-tetramethylpiperidin-1-ol (TEMPOH). Addition of either of these substrates to solutions of **2** in 2-MeTHF at −80 °C results in the rapid disappearance of 2 by UV-vis spectroscopy (Figure 7). EPR spectroscopy of the reaction mixture reveals that the $S = ½$ signal associated with **2** has disappeared, and the EPR spectrum typical of a nitroxyl radical has formed. Spin quantitations by double integration and comparison with a calibration curve indicate one equiv of both the unsubstituted and 4-OMe nitroxyl radical is formed. These results are consistent with a single H-atom transfer from the TEMPOH derivatives to the Co($O_2^{\bullet-}$) species to give TEMPO radical and a putative Co(OOH) product.

Attempts to characterize the putative Co(OOH) species by RR spectroscopy were unsuccessful, with no resonance-enhanced O_2-sensitive bands observed, which is not surprising in view of the lack of visible absorption features after exposure of **2** to TEMPOH (Figure 7). The ^{1}H NMR spectra of reaction mixtures with TEMPOH at −80 °C were also featureless, showing only residual solvent peaks. Gradual formation of precipitates in the NMR tube was evident, consistent with the absence of peaks associated with the cobalt complex. These observations suggest that the expected Co(OOH) species is unstable and decays to intractable products. For comparison, a related nonheme cobalt-hydroperoxo complex, $[Co^{III}(15\text{-TMC})(OOH)]^{2+}$, was also found to be unstable, rapidly decaying via hydroxylation of the 15-TMC ligand.[60]

Further insight into the mechanism of HAT by **2** was provided by kinetic analysis of the reaction with 4-OMe-TEMPOH. Addition of excess 4-OMe-TEMPOH(D) (12 – 60 equiv) to **2** in 2-MeTHF at −105 °C results in a first-order decay of **2** as seen by UV-vis spectroscopy. A second order rate constant of 0.87(3) M^{-1} s^{-1} was determined from the slope of a plot of k_{obs} versus [4-OMe-TEMPOH] (Figure 7). This kinetic behaviour is consistent with a second-order process for a bimolecular reaction between **2** and the substrate. A comparison of the rate constants for H versus D leads to a large kinetic isotope effect (KIE) of 8.8 at −105 °C (Figure 7). The observed KIE indicates that HAT from 4-OMe-TEMPOH to **2** is the rate-determining step.

Temperature-dependent kinetic studies were performed to provide further mechanistic information on reaction between **2** and 4-OMe-TEMPOH. An Eyring plot of ln(k/T) versus 1/T exhibits good linearity from −80 °C to −115 °C (Figure 8). The Eyring analysis yields activation parameters $\Delta H^{\ddagger}$ = 3.6 kcal mol-1 and $\Delta S^{\ddagger}$ = −46.2 cal mol-1 K-1. Small values for $\Delta H^{\ddagger}$ have been observed for H-atom abstraction reactions by other metal-superoxo complexes.[61–62] The significantly negative $\Delta S^{\ddagger}$ is indicative of an ordered transition state, and expected for a bimolecular reaction. However, the $\Delta S^{\ddagger}$ observed for the reaction of **2** with 4-OMe-TEMPOH is even more negative than most ΔS^{*} values reported for HAT reactions with TEMPOH as substrate and a range of M(OR) oxidants (M = Mn^{III}, Cu^{III}; R = H, Me, O, Cu).[62–66] This highly negative $\Delta S^{\ddagger}$ may arise from a requirement of the superoxo ligand in 2 to adopt the appropriate conformation for productive H-atom abstraction.

In contrast to the TEMPOH derivatives, stronger O-H substrates (e.g. 2,4,6-tri-tert-butylphenol, which has an O-H bond dissociation free energy (BDFE) = 80.6 kcal mol^{-1} in CH_3CN),[67] or C-H substrates (e.g. xanthene, BDFE(C-H) = 73.3 kcal mol^{-1} in DMSO)[67] are not oxidized by **2**. This lack of reactivity suggests that HAT to **2** is thermodynamically unfavorable, and implies that the strength of the O-H bond in Co(OOH) is relatively weak compared to the X-H substrates. DFT calculations to estimate the O-H bond strength in Co(OOH)(Me_3TACN)(S_2SiMe_2) were performed, and gave a BDFE(O-H) = 67 kcal mol^{-1}. This value, which is higher than the TEMPOH derivatives and lower than the stronger C-H and phenolic O-H BDFE values, is in line with the observed HAT reactivity.

To provide further experimental validation for the calculated O-H bond strength, we examined the reactivity of **2** with separated H^{+}/e^{-} donors. Individual acid/reductant pairs exhibit effective BDFE values that can be calculated from their respective pKa/E° values,[67–68] and we have previously used these effective BDFE values to bracket the O-H bond strengths of Mn^{IV}- and Cr^{IV}-hydroxo corrolazine species.[69] Addition of the acid/reductant pairs [Et_3NH]BF_4/dimethylferrocene (Me_2Fc) ($BDFE_{eff}$ = 75 kcal mol^{-1}) or [Et_3NH]BF_4/decamethylferrocene (Fc*) ($BDFE_{eff}$ = 70 kcal mol-1) results in no reaction with **2**. However, employing lutidinium tetrafluroborate/Fc* ($BDFE_{eff}$ = 63 kcal mol^{-1}) results in the decay of **2** and concomitant formation of Fc^{*+}, which gives a characteristic UV-vis feature near 780 nm (Figure S19). These results suggest that **2** can abstract H-atoms from bonds weaker than 70 kcal/mol. This upper limit is consistent with the inability to oxidize phenol O-H bonds, and the observed oxidation of TEMPOH (BDFE = 66.5 kcal mol^{-1} in CH_3CN)[67] or 4-OMe-TEMPOH (BDFE = 65.0 kcal mol-1 in CH_3CN).[67] These results are

also nicely in line with the DFT calculated BDFE of 67 kcal mol-1 for the O-H bond in the Co(OOH) product.

While **2** does not react with phenols, the related TACN-ligated superoxo complex $[Co(PyTACN)(CH_3CN)(O_2)]^{2+}$ oxidizes 2,4,6-tri-tert-butylphenol (ttbp) with a rate constant of 0.59 M^{-1} s^{-1} at −80 °C.[24] The putative cobalt(III)-hydroperoxo product was not characterized, but the oxidation of ttbp suggests that this species has a stronger O-H bond than the proposed Co(OOH) product for **2**. The dianionic, dithiolato donors in the neutral complex **2** should give a significantly less electrophilic superoxo species as compared to the dicationic PyTACN complex. The difference in electrophilicity may account for the difference in reactivity, and contribute to the proposed difference in BDFEs for the Co(OOH) species. This analysis is in line with a recent study involving a series of TMC-based $Cr^{III}(O_2^{\bullet-})$ complexes with various axial ligands, in which the most electron-poor axial donor led to the most reactive H-atom abstractor.[70]

Predictable trends for the reactivity of M-superoxo species are not well-established. Computations have suggested that electrophilicity, reaction driving force, and coupling between the metal center and superoxo ligand may play key roles in controlling the reactivity of M-superoxo species in HAT reactions.[71–72] In one computational study, it was shown that the H-atom abstraction reactivity of a series of hypothetical heme and nonheme Fe-superoxo complexes correlated with the BDE of the formed O-H bond, which increased with increasing electrophilicity of the Fe-superoxo complex.[71] More experimental studies are clearly needed to validate or refute these computational trends.

A small number of experimentally measured or calculated BDFE values for the O-H bonds of M(OOH) complexes are available, and some are tabulated in Table 2. They span a relatively wide range, with $Co(OOH)(Me_3TACN)(S_2SiMe_2)$ on the weak end. In most cases, the metal-bound species tend to exhibit significantly weakened O-H bonds compared to those for H_2O_2 or organic hydroperoxo (ROOH) species. They also tend to have weak O-H bonds compared to high-valent metal-hydroxo (M(OH)) species.71 However, some metalloenzymes are proposed to employ metal-superoxo species for abstracting H atoms from relatively strong C-H bonds.[73] For example, the ferric-superoxo intermediates in the nonheme iron enzymes IPNS and myo-inositol oxygenase (MIOX) are proposed to abstract H atoms from C-H bonds with BDE(C-H) > 90 kcal mol^{-1}.[73] More work needs to be done to determine the factors that dictate the O-H bond strengths in M(OOH) species, and control the overall oxidative potency of these metal-superoxo species.

Conclusions

We report here a new thiolate-ligated Co^{II} complex $Co^{II}(Me_3TACN)(S_2SiMe_2)$ (**1**) that reacts with O_2 to generate a mononuclear Co-superoxo complex $Co(O_2)(Me_3TACN)(S_2SiMe_2)$ (**2**). There are few examples of well-characterized thiolate-ligated metal-superoxo complexes; only two other complexes (with Fe and Co) have been described thus far.[28–29] Complex **2** was characterized structurally and spectroscopically by XAS, resonance Raman, and EPR spectroscopies, and DFT calculations supported the spectroscopic assignments. The XAS data combined with the DFT calculations suggest that the dithiolato ligation in **2**

leads to highly covalent ligand-metal bonding interactions. As a consequence, the reaction of **1** with O_2 is best described as a redox process involving the covalently bonded CoS_2 unit.

This work is the first study of HAT reactivity for a thiolate-ligated metal-superoxo complex, and it was found that H-atom abstraction occurs rather than S-oxygenation. However, complex **2** is capable of cleaving only weak O-H bonds (BDFE <70 kcal mol^{-1}). The DFT-calculated BDFE of 67 kcal mol^{-1} for the Co(OOH) product is consistent with the observed HAT reactivity, as is the experimental bracketing of the BDFE value obtained with the separated PCET reagents. In comparison, non-thiolate-ligated $Co(O_2^{\bullet-})$ species appear to be more reactive toward H-atom abstraction, possibly due to their greater electrophilicity and subsequently stronger O-H bond strengths.

The findings presented here suggest that mechanisms involving H-atom abstraction by metal-superoxo species, such as in the EgtB enzyme (Figure 1), are viable, even with the possibility of a competing S-oxygenation pathway. However, the phenolic O-H bond in EgtB is significantly stronger than the O-H bonds cleaved in this study, and suggests that the proposed $Fe^{III}(O_2^{\bullet-})$ intermediate is a more potent oxidant. In contrast, the enzyme CDO favors S-oxygenation over H-atom abstraction, even though a cross-linked cys-tyrosine group, which is a reasonable H-atom donor,[75–76] is poised near the iron center. The fundamental properties of thiolate-ligated metal-superoxo species that dictate S-oxygenation versus H-atom abstraction reactivity, and more generally, the reactivity of metal-superoxo species in biomimetic environments, warrants further examination.

EXPERIMENTAL SECTION

Materials.

All syntheses and manipulations were conducted in an N_2-filled drybox (Vacuum Atmospheres, O_2 < 0.2 ppm, H_2O < 0.5 ppm) or using standard Schlenk techniques under an atmosphere of Ar unless otherwise noted. Me_3TACN was purchased from Matrix Scientific, degassed by three freeze-pump-thaw cycles, and stored over 3 Å molecular sieves. Me_3TACN-d_9 was synthesized according to a published procedure.[53] Hexamethylcyclotrisilathiane ($(Me_2SiS)_3$) was prepared according to a published procedure.[32] $Co(OAc)_2$ was purchased from Alfa Aesar. Formalde-hyde-d_2, formic acid-d_2 in D_2O (21% w/w), and $^{18}O_2$ (98 atom %) were purchased from ICON Isotopes (Summit, N.J.). TEMPOH, 4-OMe-TEMPOH, and 4-OMe-TEMPOD were synthesized according to a published procedure.[77–78] All other reagents were purchased from commercial vendors and used without further purification. Acetonitrile, acetonitrile-d_3, and hexamethyldisiloxane were distilled from CaH_2. Tetrahydrofuran, pentane, hexane, and 2-MeTHF were dried over Na/benzophenone and subsequently distilled. Butyronitrile was distilled from Na_2CO_3/$KMnO_4$ according to a reported procedure.[79] Diethyl ether was obtained from a PureSolv solvent purification system (SPS). All solvents were degassed by a minimum of three freeze-pump-thaw cycles and stored over freshly activated 3 Å molecular sieves in the drybox following distillation.

Instrumentation.

The ^{1}H spectra were measured on a Bruker 300 MHz or a Bruker 400 MHz spectrometer. ^{2}H NMR spectra were recorded with a broad-band coil on a 300 MHz instrument with ^{2}H resonance at 46 MHz. Solution magnetic susceptibilities were determined by a simplified Evans method.[80–81] Chemical shifts were referenced to reported solvent resonances.[82] UV-vis experiments were carried out on a Cary bio-50 or Cary 60 UV-Vis Spectrophotometer equipped with a Unisoku USP-203A cryostat using a 1 cm modified Schlenk cuvette. Midwest Microlab (Indianapolis, IN) conducted elemental analyses on samples prepared and shipped in ampules sealed under vacuum. EPR measurements were performed on a Bruker X-band EPR in 5 mm quartz EPR tubes (Willmad). EPR Spectral simulations were performed using *EasySpin*.[83] Infrared spectra were recorded on a ThermoNicolet Nexus 670 FTIR Spectrometer with an ATR diamond crystal stage using the OMNIC 6.0a software package. Infrared spectra were collected on crystalline solids that were crushed into a fine powder. Cyclic voltammetry experiments were performed in a N2 atmosphere glovebox using a Princeton Applied Research Versastat II potentiostat and a three-electrode setup (2 mm glassy carbon working electrode, Pt wire counter electrode, and $Ag/AgNO_3$ reference electrode) with electrodes purchased from BASi, Inc., and/or CH Instruments, Inc.

Computational Methods.

All geometry optimizations were performed in the *ORCA-4.0.1.2* program package.[84] Initial geometries were obtained from the X-ray crystallo-graphic model of **1** and altered as needed. Optimized geometries were calculated using the BP86 functional[85–86] in com bination with the D3 dispersion correction.[87] The triple-ξ basis set (def2-TZVP)[88–90] was used for all Co, S, N, O, and Si atoms, and the def2-SVP basis set was used for all C and H atoms. Solvent effects in these calculations were accounted for by using the conductor-like polarizable continuum model (CPCM), specifying the dielectric constant (ε) for THF in all cases.[91] To reduce computational costs, the resolution of identity and chain of sphere (RIJCOSX) approximations[92] in tandem with the def2/J auxiliary basis set[93] were employed. Due to SCF convergence difficulties in some cases, damping parameters were altered using the slowconv function in ORCA. Frequency calculations at the same level of theory confirmed that all optimizations had converged to true minima on the potential energy surface (i.e., no imaginary frequencies). Single point calculations were carried out using the B3LYP[94] hybrid density functional to generate quasi-restricted molecular orbitals (QROs).[95] These calculations employed zeroth order regular approximation (ZORA)[96–98] for relativistic effects. Single point calculations used the CP(PPP)[99–100] basis set on Co and the ZORA-def2-TZVP(-f)[88–90] basis set on all other atoms. Molecular orbitals were visualized in UCSF Chimera *1.10*.[101] Bond dissociation free energies were calculated at 1 atm and 25 °C using the geometry optimization and frequency calculations performed with BP86. Corrections for vibrational, zero-point energy, and contributions from translational, rotational, and vibrational modes to the energy and entropy of the H-atom transfer were accounted for. The electronic energy of $H^{\bullet}$ used in the calculation of the BDFEs is 313.1 kcal mol^{-1}.

Synthesis of $Co^{II}(Me_3TACN)(S_2SiM_{e2})$ (1).

To a solution of Me_3TACN (159 mg, 0.926 mmol) in THF (~ 4 mL) was added $Co(OA_c)_2$ (164 mg, 0.926 mmol) to afford a purple slurry. The slurry was heated to 60 °C until all the solids are dissolved, affording a purple solution, which was then allowed to cool to 24 °C. A solution of hexamethylcyclotrisilathiane (251 mg, 0.926 mmol) in hexane (~ 2 mL) was added dropwise to the purple solution resulting in a rapid color change to dark green and the formation of a green precipitate. The reaction was allowed to stir for 2 h, and the precipitate was allowed to settle. The solution was removed from the precipitate, which was then washed twice with Et_2O. The remaining blue solid was dried and redissolved in minimal THF. Vapor diffusion of pentane afforded **1** as green/blue crystals after 48 h (171 mg, 52%) UV-vis (2-MeTHF): λ_{max} = 287 nm (ε = 3650 M^{-1} cm^{-1}), 347 nm (ε = 1150 M^{-1} cm^{-1}), 404 nm (ε = 1300 M^{-1} cm^{-1}), 483 nm (ε = 300 M^{-1} cm^{-1}), 604 nm (ε = 200 M^{-1} cm^{-1}), 751 nm (ε = 100 M^{-1} cm^{-1}). Selected IR bands, ν (cm^{-1}): 2889, 1499, 1447, 1295, 1060, 1009, 826, 783, 666. ^1H NMR: (CD_3CN, 400 MHz): δ 96.03, 20.60, −52.46 ppm. Evans method (CD_3CN, 400 MHz): μ_{eff} = 4.89 μ_B. Anal. Calcd for $C_{11}H_{27}N_3S_2Co$: C, 37.48; H, 7.72; N, 11.92. Found: C, 37.16; H, 7.52; N, 11.50. $Co^{II}(Me_3TACN\text{-}d_9)(S_2SiM_{e2})$ (**1-*d*$_9$**) was synthesized using the same procedure as that for **1** using Me_3TACN-d_9.

Titration of Dioxygen to Generate 2 as Monitored by UV-vis Spectroscopy.

An O_2 saturated solution of 2-MeTHF was prepared by sparging 2-MeTHF with dry O_2 for 30 min at 40 °C (5.75 mM).[102] The O_2 saturated solution was drawn into a gas-tight syringe and added in 50 μL (0.19 equiv) aliquots to a solution of **1** in 2-MeTHF (2.45 mL, 0.614 mM) at −135 °C. Following addition of 0.88 equiv, excess O_2 was bubbled into the solution to fully generate **2**. The formation of **2** was monitored by observing the growth of the band at 555 nm, and full formation was reached with ~1 equiv of O_2, consistent with the formation of a 1:1 Co/O_2 species.

Preparation of Resonance Raman Samples.

A stock solution of $Co^{II}(Me_3TACN)(S_2SiM_{e2})$ (**1**) was prepared in 2-MeTHF (2.6 mM). An aliquot of the stock solution of 1 was transferred in to a 5 mm NMR tube and sealed with a septum in a drybox. The sealed NMR tube was removed from the drybox and cooled to −135 °C in a pentane/N_2(l) bath. Using a 3-way gas-tight syringe, 2 mL of $^{16}O_2$ (natural abundance) or $^{18}O_2$ (98%) was added to the solution of **1**, yielding a color change from pale purple to dark orange. The reaction was allowed to proceed with frequent manual mixing for 5 min, and then the reaction mixture was slowly annealed in liquid nitrogen and stored at 77 K until needed.

Resonance Raman spectra were obtained on samples maintained at 110 K using a backscattering geometry and a McPherson 2061/207 spectrograph equipped with a liquid-nitrogen-cooled CCD camera (LN-1100PB, Princeton Instruments). The 407-nm excitation was derived from a Kr laser (Innova 302C, Coherent). Frequencies were calibrated using aspirin and are accurate to ± 1 cm^{-1}. The photosensitivity of **2** was assessed as minimal by comparing short data acquisition with laser powers ranging from 5 to 20 mW and continuous spinning of the samples in NMR tubes.

Preparation of XAS Samples.

A stock solution of $Co^{II}(Me_3TACN)(S_2SiM_{e2})$ (**1**) was prepared in 2-MeTHF (4 mL, 6 mM). An aliquot of this stock solution (300 μL) was transferred in a drybox to an XAS cell with slit width 9 × 2 mm. The slits were covered with Kapton tape (38 μm thickness) to make X-ray transparent windows. The XAS cell was sealed in a vial, removed from the drybox, and the vial was submerged in liquid nitrogen. For preparation of the super-oxo complex **2**, approximately 2 mL of the stock solution of **1** was sealed in a vial and subsequently cooled to −135 °C. Excess O_2 was added to the pale purple solution resulting in a color change to dark orange. The reaction mixture was stirred for 5 min, and then quickly poured into a small volume of liquid nitrogen to produce a frozen orange powder. The powder was pulverized with a spatula while being maintained under liquid nitrogen, and then transferred to a Delrin XAS cup with slits (1 × 4 mm). The slits were covered with Kapton tape (38 μm) to make X-ray transparent windows.

Co K-edge XAS data were obtained at the Stanford Synchrotron Radiation Lightsource under ring conditions of 3.0 GeV and 500 mA. Data were obtained at either beamline 93 (**1**) or 7–3 (**2**). In both cases, incident energy selection was achieved using Si(220) double-crystal monochromators, and harmonics were rejected using Rh-coated mirrors set to an energy cutoff of 9000 eV. Data were collected in fluorescence mode using either a Lytle detector (**1**) or a Canberra 30-element solid state Ge detector windowed on Co Kα emission. Samples were maintained at 10 K in a liquid He flow cryostat. Internal energy calibration was performed by assigning the first inflection point of a Co foil spectrum to 7709.5 eV. Data represent 4 scan averages. Spectra were processed using the SIXPACK software package.[103] A second-order polynomial was fit to the pre-edge region, and this background was subtracted from the entire spectrum. A three-region cubic spline was used to model the smooth background above the edge. Data were normalized by subtracting this spline and normalizing the post edge (7750 eV) to 1.0. EXAFS data were fit using the OPT module of EXAFSPAK[104] with input scattering paths calculated using FEFF7.[105–106]

Preparation of EPR Samples for Quantitation of TEMPO Radical Derivatives.

A stock solution of Co^{II} $(Me_3TACN)(S_2SiM_{e2})$ (**1**) was prepared in 2-MeTHF (1.23 mM). An aliquot of the stock solution (450 μL) of **1** was transferred into a 5 mm EPR tube and sealed with a septum in a drybox. The tube was removed from the drybox and cooled to −80 °C. Excess O_2 was then bubbled directly through the solution of **1** resulting in a color change from purple to orange, and the solution was then deoxygenated by sparging with Ar(g) for 1 min. An amount of TEMPOH or 4-OMe-TEMPOH (25 or 50 μL; 2.5 or 5 equiv) was added to the reaction mixture and the reaction was allowed to proceed for 25 min with frequent manual mixing. Samples were then slowly annealed in liquid nitrogen and stored at 77 K until needed.

Kinetic Studies.

$Co(M_{e3}TACN)(S_2SiM_{e2})(O_2)$ (**2**) was generated *in situ* by bubbling excess O_2 through a solution of **1** in 2-MeTHF (0.525 mM, 1.95 mL) at the desired temperature. Following full formation of 2, the solution was deoxygenated by sparging with Ar(g) for 10 min. Varying

amounts of 4-OMe-TEMPOH (5.8 mM - 29.0 mM) were added, resulting in the decay of **2** as monitored by UV-vis spectroscopy. The pseudo-first-order rate constants (k_{obs}) for these reactions were obtained by non-linear least-squares fitting of the plots of absorbance at 554 nm (Abs_t) versus time (t) according to the equation $Abs_t = Abs_f + (Abs_0 - Abs_f) \exp(-k_{obs}t)$ where Abs_0 and Abs_f are initial and final absorbance, respectively. Second order rate constants (k) were obtained from the slope of the best-fit line from a plot of k_{obs} versus substrate concentration.

Supplementary Material

Refer to Web version on PubMed Central for supplementary material.

ACKNOWLEDGMENT

The NIH (GM119374to D.P.G. and P.M.L. and R35GM124908 to K.M.L.) is gratefully acknowledged for financial support. This work was also supported by an A. P. Sloan Research Fellowship to K.M.L. Computer time was provided by the Maryland Advanced Research Computing Center (MARCC). XAS data were obtained at SSRL, which is supported by the U.S. Department of Energy, Office of Science, Office of Basic Energy Sciences under Contract No. DE-AC02–76SF00515. The SSRL Structural Molecular Biology Program is supported by the Department of Energy's Office of Biological and Environmental Research, and by NIH/NIGMS (including P41GM103393).

REFERENCES

(1). Sahu S; Goldberg DP J. Am. Chem. Soc 2016, 138, 11410-11428. [PubMed: 27576170] -

(2). Costas M; Mehn MP; Jensen MP; Que L Jr. Chem. Rev 2004, 104, 939-986. [PubMed: 14871146] -

(3). Wang D; Weinstein AB; White PB; Stahl SS Chem. Rev 2018, 118, 2636-2679. [PubMed: 28975795] -

(4). Campbell AN; Stahl SS Acc. Chem. Res 2012, 45, 851-863. [PubMed: 22263575] -

(5). Shao M; Chang Q; Dodelet J-P; Chenitz R Chem. Rev 2016, 116, 3594-3657. [PubMed: 26886420] -

(6). Tamanaha E; Zhang B; Guo Y; Chang W.-c.; Barr EW; Xing G; St. Clair J; Ye S; Neese F; Bollinger JM Jr.; Krebs C J. Am. Chem. Soc 2016, 138, 8862-8874. [PubMed: 27193226] -

(7). Tchesnokov EP; Faponle AS; Davies CG; Quesne MG; Turner R; Fellner M; Souness RJ; Wilbanks SM; de Visser SP; Jameson GNL Chem. Commun 2016, 52, 8814-8817.-

(8). Kumar D; Thiel W; de Visser SP J. Am. Chem. Soc 2011, 133, 3869-3882. [PubMed: 21344861] -

(9). Aluri S; de Visser SP J. Am. Chem. Soc 2007, 129, 14846-14847. [PubMed: 17994747] -

(10). Chen L; Naowarojna N; Song H; Wang S; Wang J; Deng Z; Zhao C; Liu PJ Am. Chem. Soc 2018, 140, 4604-4612.-

(11). Faponle AS; Seebeck FP; de Visser SP J. Am. Chem. Soc 2017, 139, 9259-9270. [PubMed: 28602090] -

(12). Goncharenko KV; Seebeck FP Chem. Commun 2016, 52, 1945-1948.-

(13). Bailey CL; Drago RS Coord. Chem. Rev 1987, 79, 321-332.-

(14). Kothari VM; Tazuma JJ J. Catal 1976, 41, 180-189.-

(15). Nishinaga A; Nishizawa K; Tomita H; Matsuura T J. Am***. Chem. Soc***. 1977, 99, 1287-1288. [PubMed: 833407] -

(16). Zombeck A; Drago RS; Corden BB; Gaul JH J. Am. Chem. Soc 1981, 103, 7580-7585.-

(17). Nishinaga A; Tomita H; Nishizawa K; Matsuura T; Ooi S; Hirotsu K J. Chem. Soc., Dalton Trans. 1981, 1504-1514.-

(18). Wang X-Y; Motekaitis RJ; Martell AE Inorg. Chem 1984, 23, 271-275.-

(19). Corden BB; Drago RS; Perito RP J. Am. Chem. Soc 1985, 107, 2903-2907.-

(20). Deng Y; Busch DH Inorg. Chem 1995, 34, 6380-6386.-

(21). Musie GT; Wei M; Subramaniam B; Busch DH Inorg. Chem 2001, 40, 3336-3341. [PubMed: 11421677] -

(22). Wang C-C; Chang H-C; Lai Y-C; Fang H; Li C-C; Hsu HK; Li Z-Y; Lin T-S; Kuo T-S; Neese F; Ye S; Chiang Y-W;Tsai M-L; Liaw W-F; Lee W-Z J. Am. ***Chem. Soc***. 2016, 138, 14186-14189. [PubMed: 27726348] -

(23). Chiang C-W; Kleespies ST; Stout HD; Meier KK; Li PY; Bominaar EL; Que L Jr.; Münck E; Lee W-Z J. ***Am. Chem. Soc***. 2014, 136, 10846-10849. [PubMed: 25036460] -

(24). Corona T; Padamati SK; Acuña-Parés F; Duboc C; Browne WR; Company A Chem. Commun 2017, 53, 11782-11785.-

(25). Oddon F; Chiba Y; Nakazawa J; Ohta T; Ogura T; Hikichi S Angew. Chem., Int. Ed. Engl 2015, 54, 7336-7339. [PubMed: 25940278] -

(26). Hong S; Sutherlin KD; Park J; Kwon E; Siegler MA; Solomon EI; Nam W Nat. Commun 2014, 5, 5440. [PubMed: 25510711]

(27). Corcos AR; Villanueva O; Walroth RC; Sharma SK; Bacsa J; Lancaster KM; MacBeth CE; Berry JF J. Am. Chem. Soc 2016, 138, 1796-1799. [PubMed: 26799113] -

(28). Fischer AA; Lindeman SV; Fiedler AT Dalton Trans. 2017, 46, 13229-13241. [PubMed: 28686274] -

(29). Fischer AA; Lindeman SV; Fiedler AT Chem. Commun 2018, 54, 11344-11347.-

(30). Penfield KW; Gewirth AA; Solomon EI J. Am. Chem. Soc 1985, 107, 4519-4529.-

(31). Addison AW; Rao TN; Reedijk J; van Rijn J; Verschoor GC J. Chem. Soc., Dalton Trans 1984, 1349-1356.-

(32). Komuro T; Matsuo T; Kawaguchi H; Tatsumi K Inorg. Chem 2003, 42, 5340-5347. [PubMed: 12924906] -

(33). Brines LM; Shearer J; Fender JK; Schweitzer D; Shoner SC; Barnhart D; Kaminsky W; Lovell S; Kovacs JA Inorg. Chem 2007, 46, 9267-9277. [PubMed: 17867686] -

(34). Shoner SC; Nienstedt AM; Ellison JJ; Kung IY; Barnhart D; Kovacs JA Inorg. Chem 1998, 37, 5721-5726.-

(35). Brines LM; Villar-Acevedo G; Kitagawa T; Swartz RD; Lugo-Mas P; Kaminsky W; Benedict JB; Kovacs JA Inorg. Chim Acta 2008, 361, 1070-1078.-

(36). Scarpellini M; Wu AJ; Kampf JW; Pecoraro VL Inorg. Chem 2005, 44, 5001-5010. [PubMed: 15998028] -

(37). Holland PL; Cundari TR; Perez LL; Eckert NA; Lachicotte RJ J. Am. Chem. Soc 2002, 124, 14416-14424. [PubMed: 12452717] -

(38). Ding K; Dugan TR; Brennessel WW; Bill E; Holland PL Organometallics 2009, 28, 6650-6656.-

(39). Lodeiro C; Capelo JL; Bértolo E; Bastida R Z. A***norg. Allg. Chem.*** 2004, 630, 1110-1115.-

(40). Wang Y-H; Pegis ML; Mayer JM; Stahl SS J. Am. Chem. Soc 2017, 139, 16458-16461. [PubMed: 29039921] -

(41). Bajdor K; Nakamoto K; Kanatomi H; Murase I Inorg. Chim. Acta 1984, 82, 207-210.-

(42). Bajdor K; Kincaid JR; Nakamoto KJ Am. Chem. Soc 1984,106, 7741-7747.-

(43). Mittra K; Mondal B; Mahammed A; Gross Z; Dey A Chem. Commun 2017, 53, 877-880.-

(44). Tsubaki M; Yu N-T Proc. Natl. Acad. Sci. U. S. A 1981, 78, 3581-3585. [PubMed: 6943559] -

(45). Nakamoto K, Infrared and Raman Spectra of Inorganic and Coordination Compounds, Theory and Applications in Inorganic Chemistry. Wiley: 1997.

(46). Spaeth AD; Gagnon NL; Dhar D; Yee GM; Tolman WB J. Am. Chem. Soc 2017, 139, 4477-4485. [PubMed: 28319386] -

(47). Jones RD; Summerville DA; Basolo F Chem. Rev 1979, 79, 139-179.-

(48). Smith TD; Pilbrow JR Coord. Chem. Rev 1981, 39, 295-383.-

(49). Fielding AJ; Lipscomb JD; Que L Jr.J. Am. Chem. Soc 2012,134, 796-799. [PubMed: 22175783] -

(50). MacMillan SN; Lancaster KM ACS Catalysis 2017, 7, 1776-1791.-

(51). Kau L-S; Spira-Solomon DJ; Penner-Hahn JE; Hodgson KO; Solomon EI J. Am. Chem. Soc 1987, 109, 6433-6442.-

(52). Siegbahn PEM J. Biol. Inorg. Chem 2006, 11, 695-701. [PubMed: 16830147]

(53). Gordon JB; McGale JP; Prendergast JR; Shirani-Sarmazeh Z; Siegler MA; Jameson GNL; Goldberg DP J. Am. Chem. Soc 2018, 140, 14807-14822. [PubMed: 30346746] -

(54). McQuilken AC; Goldberg DP Dalton Trans. 2012, 41, 10883-10899. [PubMed: 22814765] -

(55). McQuilken AC; Jiang Y; Siegler MA; Goldberg DP J. Am. Chem. Soc 2012, 134, 8758-8761. [PubMed: 22578255] -

(56). Fischer AA; Stracey N; Lindeman SV; Brunold TC; Fiedler AT Inorg. Chem 2016, 55, 11839-11853. [PubMed: 27801576] -

(57). Sallmann M; Braun B; Limberg C Chem. Commun 2015, 51, 6785-6787.-

(58). Sallmann M; Siewert I; Fohlmeister L; Limberg C; Knispel C Angew. Chem., Int. Ed. Engl 2012, 51, 2234-2237. [PubMed: 22287034] -

(59). Villar-Acevedo G; Lugo-Mas P; Blakely MN; Rees JA; Ganas AS; Hanada EM; Kaminsky W; Kovacs JA J. Am. Chem. Soc 2017, 139, 119-129. [PubMed: 28033001] -

(60). Kim D; Cho J; Lee Y-M; Sarangi R; Nam W Chem. Eur. J 2013, 19, 14112-14118. [PubMed: 24038300] -

(61). Lee JY; Peterson RL; Ohkubo K; Garcia-Bosch I; Himes RA; Woertink J; Moore CD; Solomon EI; Fukuzumi S; Karlin KD J. Am. Chem. Soc 2014, 136, 9925-9937. [PubMed: 24953129] -

(62). Kindermann N; Günes C-J; Dechert S; Meyer F J. ***Am. Chem. Soc***. 2017, 139, 9831-9834. [PubMed: 28691811] -

(63). Coggins MK; Brines LM; Kovacs JA Inorg. Chem 2013, 52, 12383-12393. [PubMed: 24156315] -

(64). Rice DB; Jones SD; Douglas JT; Jackson TA Inorg. Chem 2018, 57, 7825-7837. [PubMed: 29927591] -

(65). Wijeratne GB; Day VW; Jackson TA Dalton Trans. 2015, 44, 3295-3306. [PubMed: 25597362] -

(66). Ali G; VanNatta PE; Ramirez DA; Light KM; Kieber-Emmons MT J. Am. Chem. Soc 2017, 139, 18448-18451. [PubMed: 29207870] -

(67). Warren JJ; Tronic TA; Mayer JM Chem. Rev 2010, 110, 6961-7001. [PubMed: 20925411] -

(68). Waidmann CR; Miller AJM; Ng C-WA; Scheuermann ML; Porter TR; Tronic TA; Mayer JM Energy Environ. Sci 2012, 5, 7771-7780.-

(69). Baglia RA; Prokop-Prigge KA; Neu HM; Siegler MA; Goldberg DP J. Am. Chem. Soc 2015, 137, 10874-10877. [PubMed: 26295412] -

(70). Goo YR; Maity AC; Cho K-B; Lee Y-M; Seo MS; Park YJ; Cho J; Nam W Inorg. Chem 2015, 54, 10513-10520. [PubMed: 26486819] -

(71). Chung LW; Li X; Hirao H; Morokuma K J. ***Am. Chem. Soc***. 2011, 133, 20076-20079. [PubMed: 22047171] -

(72). Ansari A; Jayapal P; Rajaraman G Angew. Chem., Int. Ed. Engl 2015, 54, 564-568. [PubMed: 25418430] -

(73). Bollinger JM Jr.; Krebs C Curr. Opin. Chem. Biol 2007, 11, 151-158. [PubMed: 17374503] -

(74). Latifi R; Tahsini L; Nam W; de Visser SP Phys. Chem. Chem. Phys 2012, 14, 2518-2524. [PubMed: 22252092] -

(75). Whittaker JW Chem. Rev 2003, 103, 2347-2363. [PubMed: 12797833]

(76). Amorati R; Catarzi F; Menichetti S; Pedulli GF; Viglianisi C J. ***Am. Chem. Soc***. 2008, 130, 237-244. [PubMed: 18072772] -

(77). Mader EA; Davidson ER; Mayer JM J. Am. Chem. Soc 2007, 129, 5153-5166. [PubMed: 17402735] -

(78). Wu A; Mader EA; Datta A; Hrovat DA; Borden WT; Mayer JM J. Am. Chem. Soc 2009, 131, 11985-11997. [PubMed: 19618933] -

(79). Armarego WLF; Chai CLL, Purification of Laboratory Chemicals. 6th ed; Elsevier/Butterworth-Heinemann: Amsterdam ; Boston, 2009.

(80). Evans DF; Jakubovic DA J. Chem. Soc., Dalton Trans 1988, 2927-2933.-

(81). Evans DF J. Chem. Soc 1959, 2003-2005.
(82). Fulmer GR; Miller AJM; Sherden NH; Gottlieb HE; Nudelman A; Stoltz BM; Bercaw JE; Goldberg KI Organometallics 2010, 29, 2176-2179.-
(83). Stoll S; Schweiger A Journal of Magnetic Resonance 2006, 178, 42-55. [PubMed: 16188474] -
(84). Neese F WIREs Comput. Mol. Sci 2012, 2, 73-78.
(85). Perdew JP Phys. Rev. B 1986, 33, 8822-8824.
(86). Becke AD Phys. Rev. A 1986, 33, 2786-2788.
(87). Grimme S; Antony J; Ehrlich S; Krieg H J. ***Chem. Phys***. 2010, 132, 154104. [PubMed: 20423165]
(88). Weigend F; Ahlrichs R Phys. Chem. Chem. Phys 2005, 7, 3297-3305. [PubMed: 16240044] -
(89). Schäfer A; Horn H; Ahlrichs R J. C***hem. Phys***. 1992, 97, 2571-2577.-
(90). Schäfer A; Huber C; Ahlrichs R J. C***hem. Phys***. 1994, 100, 5829-5835.-
(91). Marenich AV; Cramer CJ; Truhlar DG J. Phys. Chem. B 2009, 113, 6378-6396. [PubMed: 19366259] -
(92). Neese F; Wennmohs F; Hansen A; Becker U Chem. Phys 2009, 356, 98-109.-
(93). Eichkorn K; Treutler O; Öhm H; Häser M; Ahlrichs R Chem. Phys. Lett 1995, 240, 283-290.-
(94). Stephens PJ; Devlin FJ; Chabalowski CF; Frisch MJ J. Chem. Phys 1994, 98, 11623-11627.-
(95). Neese F J. ***Am. Chem. Soc***. 2006, 128, 10213-10222. [PubMed: 16881651]
(96). Lenthe E. v.; Baerends EJ; Snijders JG J. Chem. Phys 1993, 99, 4597-4610.-
(97). Lenthe E. v. ; Baerends EJ; Snijders JG J. Chem. Phys 1994, 101, 9783-9792.-
(98). Wüllen C. v J. Chem. Phys 1998, 109, 392-399.
(99). Neese F Inorg. Chim. Acta 2002, 337, 181-192.
(100). Hedegård ED; Kongsted J; Sauer SPAPhys. Chem. Chem. Phys 2012, 14, 10669-10676. [PubMed: 22785432] -
(101). Pettersen EF; Goddard TD; Huang CC; Couch GS; Greenblatt DM; Meng EC; Ferrin TE J. Comput. Chem 2004, 25, 1605-1612. [PubMed: 15264254] -
(102). Saracini C; Liakos DG; Zapata Rivera JE; Neese F; Meyer GJ; Karlin KD J. Am. Chem. Soc 2014, 136, 1260-1263. [PubMed: 24428309] -
(103). Webb SM Phys. Scr 2005, 2005, 1011.
(104). George GN. EXAFSPAK. Stanford Synchrotron Radiation Lightsource, S. L. A. C., Stanford University.
(105). Mustre de Leon J; Rehr JJ; Zabinsky SI; Albers RC Phys. Rev. B 1991, 44, 4146-4156.-
(106). Rehr JJ; Mustre de Leon J; Zabinsky SI; Albers RC J. Am. Chem. Soc 1991, 113, 5135-5140.-

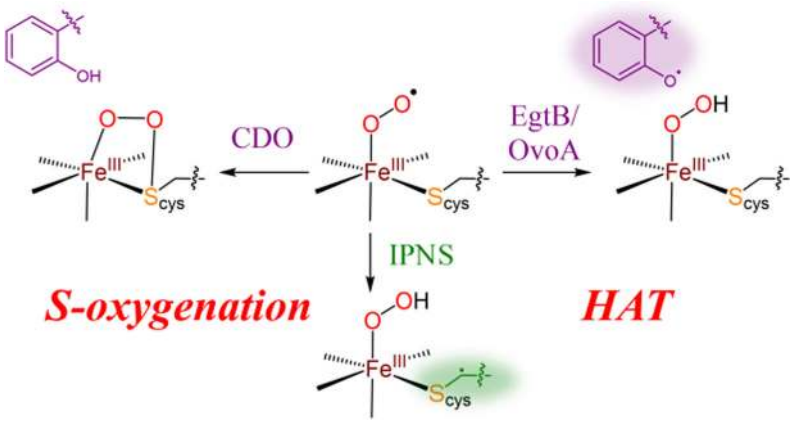

Figure 1.
Divergent reactivity performed by nonheme Fe thio-late-ligated enzymes.

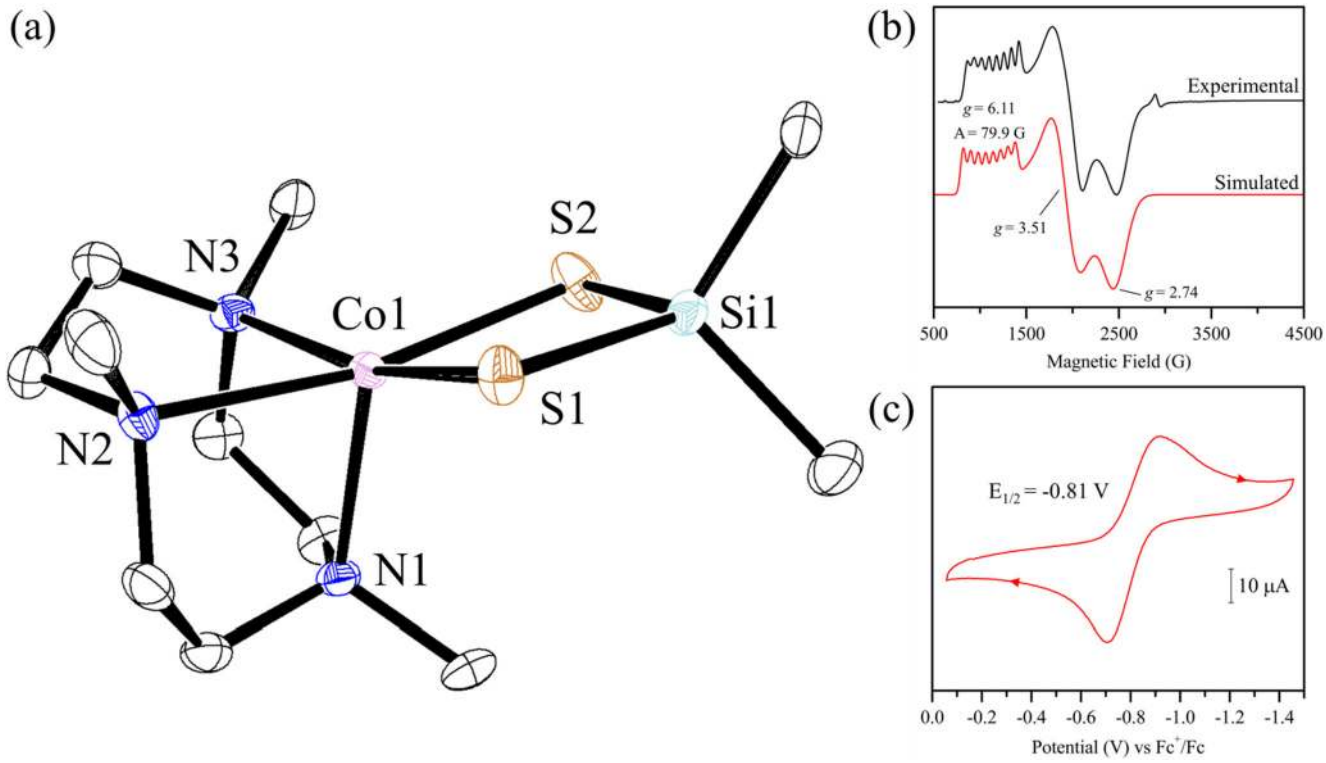

Figure 2.

(a) Displacement ellipsoid plot (50% probability level) for **1** at 110(2) K. Hydrogen atoms have been omitted for clarity. Selected bond distances (Å): Co1-S1, 2.3928(8), Co1-S2, 2.3498(9), Co1-N1, 2.121(3), Co1-N2, 2.222(3), Co1-N3, 2.218(3). (b) X-band EPR spectrum of **1** (2 mM) in butyronitrile at 12 K (black line) and simulation (red line). Conditions: microwave freq. = 9.415912 GHz; microwave power = 0.20 mW; modulation amp. = 10 G; receiver gain = 5×10^3. (c) Cyclic voltammogram of **1** (3 mM) in butyronitrile at 23 °C, using 0.3 M $^{n}B_{u4}NPF_6$ as supporting electrolyte. Working electrode: glassy carbon; reference electrode: $Ag/AgNO_3$; counter electrode: Pt wire. Scan rate: 0.2 V/s.

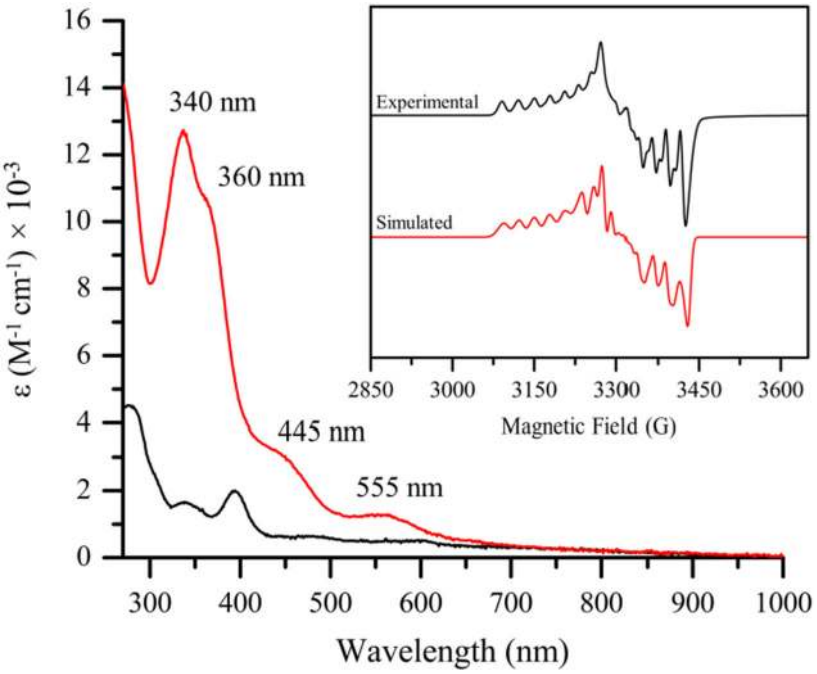

Figure 3.

UV-vis spectra of **1** (black line) and **2** (red line) in 2-MeTHF. Inset: X-band EPR spectrum of **2** (2 mM) in 2-MeTHF at 12 K (black line) and simulation (red line). Conditions: Microwave frequency = 9.420351 GHz; microwave power = 0.20 mW; modulation amp. = 10 G; receiver gain = 5×10^3.

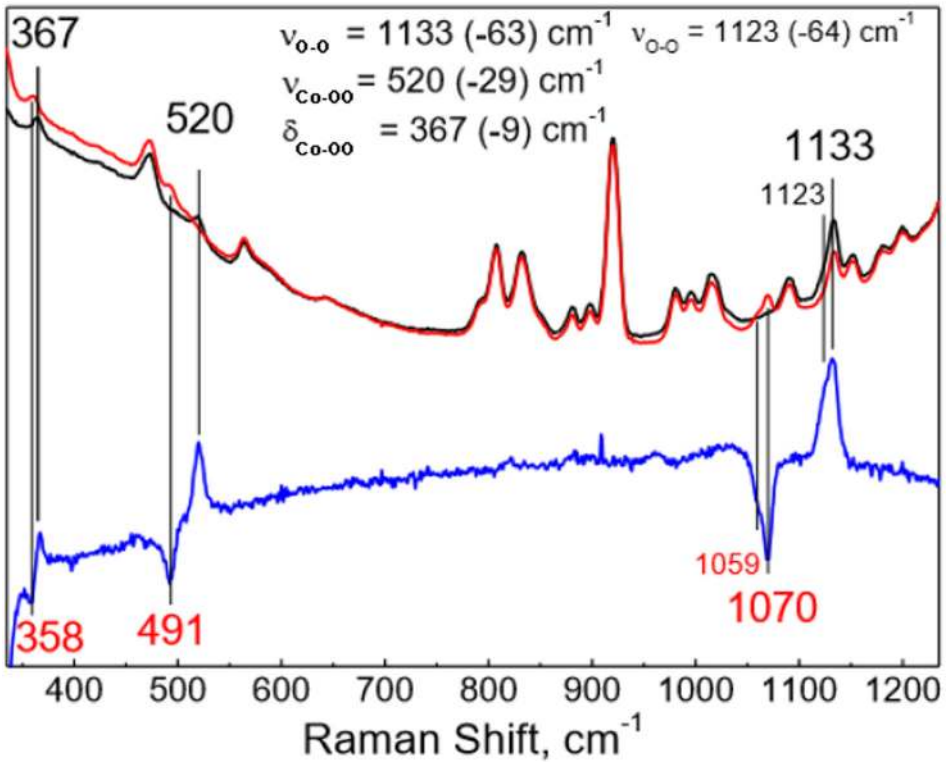

Figure 4.

Resonance Raman spectra of **2** in 2-MeTHF at 110 K (λ_{exc} = 407 nm). Black spectrum for **2** with $^{16}O_2$ (natural abundance); red spectrum for **2** with $^{18}O_2$ (98%); blue spectrum is the difference spectrum ($^{16}O_2$ - $^{18}O_2$).

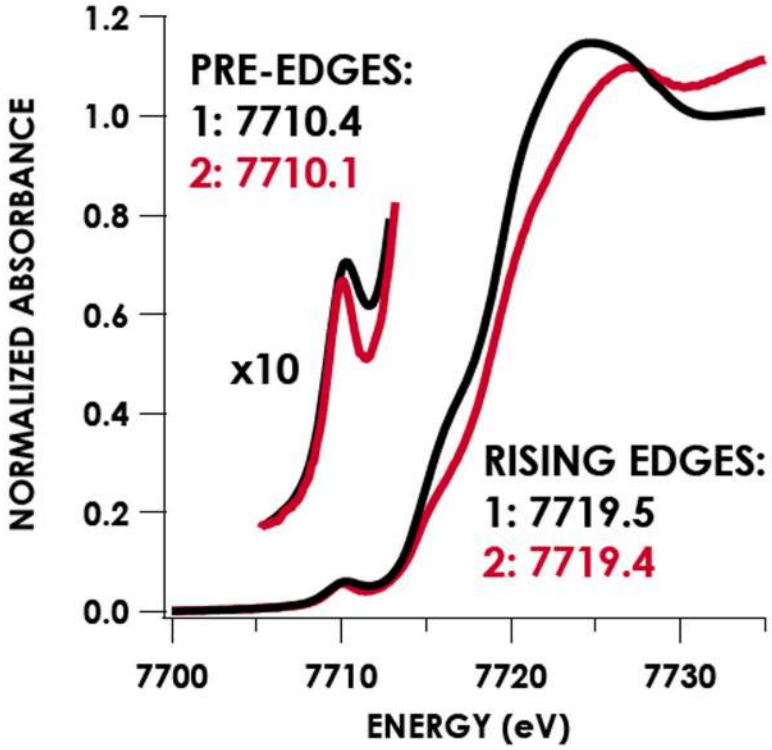

Figure 5.
Co K-edge XAS data obtained for **1** (black) and **2** (red). Data were collected on 2-MeTHF solution frozen at 10 K.

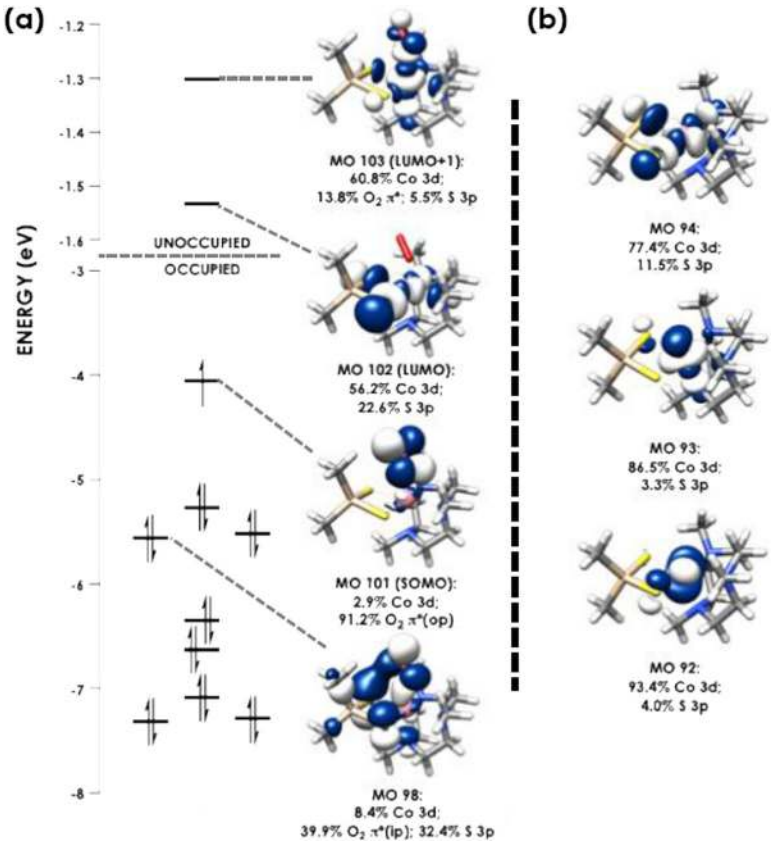

Figure 6.

(a) Molecular orbital diagram for **2** obtained from quasi-restricted DFT (B3LYP, CP(PPP) on Co, ZORA-def2-TZVP(-f) on all other atoms. (b) Singly occupied molecular orbitals for **1** obtained using the same calculational approach as in (a). Isosurfaces are plotted at values of +/−0.03 a.u.

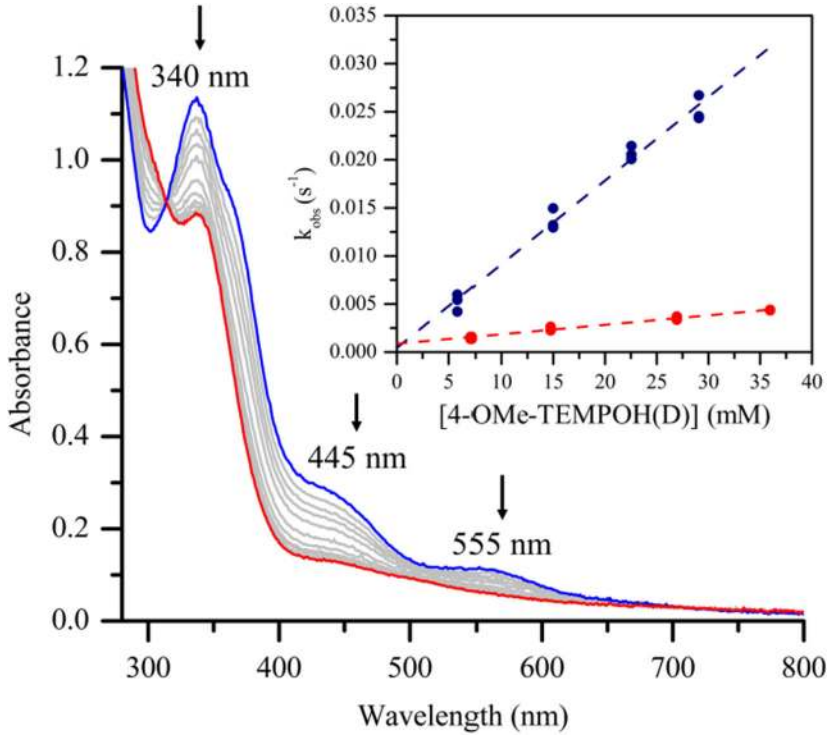

Figure 7.

UV-vis spectra showing decay of **2** (0.53 mM) in 2-MeTHF (blue line) following addition of excess 4-OMe-TEMPOH at −80 °C, with grey lines denoting 14 s intervals. Inset: Plot of k_{obs} versus [4-OMe-TEMPOH] (blue points) and [4-OMe-TEMPOD] (red points) at −105 °C. Best fits are shown as blue and red dashed lines, yielding second order rate constants of 0.87(3) M^{-1} s^{-1} and 0.098(6) M^{-1} s^{-1}, respectively.

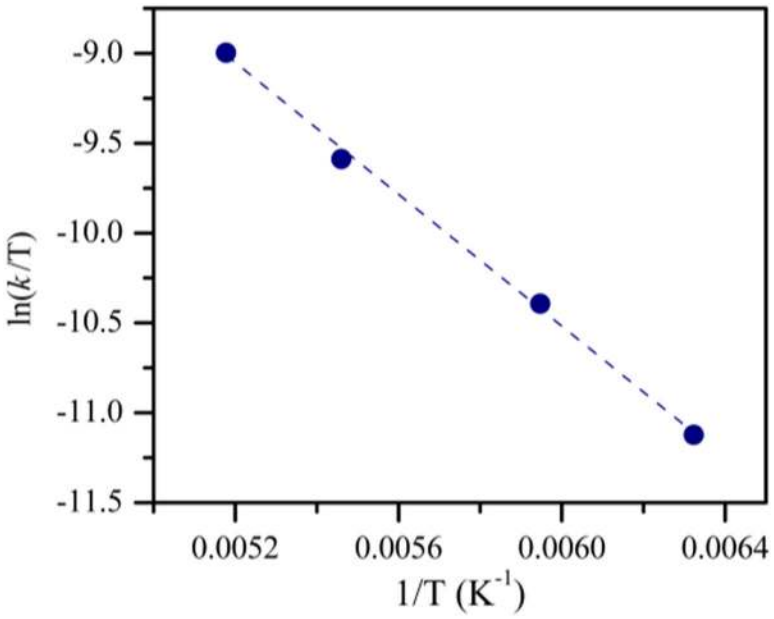

Figure 8.

Eyring plot for the reaction of **2** (0.53 mM) with 4-OMe-TEMPOH (6 mM) in 2-MeTHF from −80 °C to −115 °C.

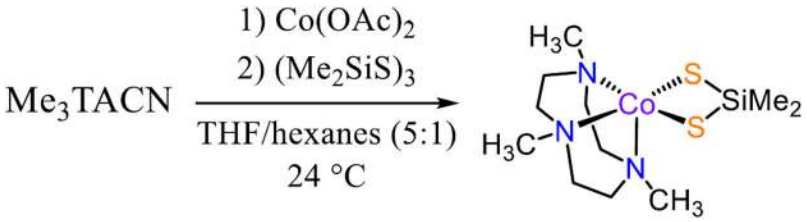

Scheme 1.
Synthesis of 1

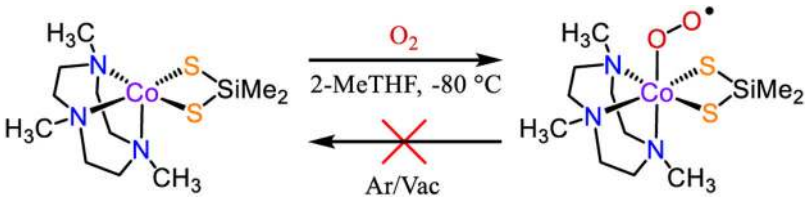

Scheme 2.
Reaction of 2 with O_2

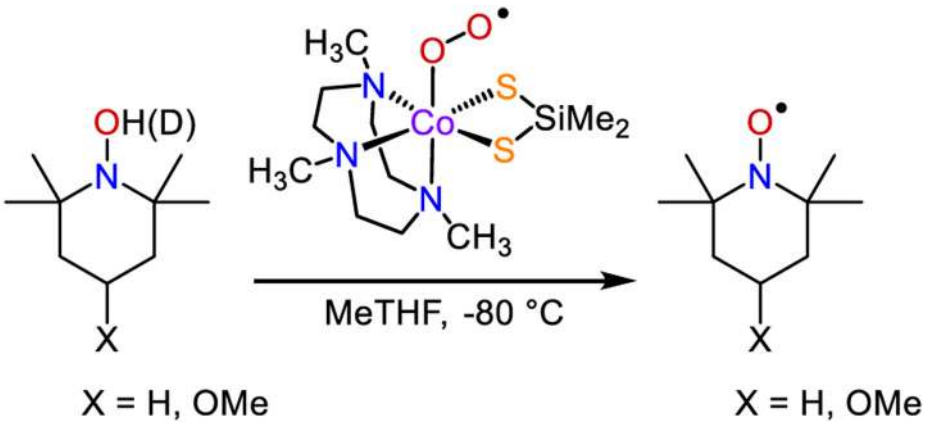

Scheme 3.
Reaction of 2 with TEMPOH derivatives

Table 1.

Vibrational data (cm^{-1}) for selected Co-super-oxo species[a]

Complex	ν(O–O)	Δ(^{18}O)	ν(Co–O)	Δ(^{18}O)
$Co(O_2)(Me_3TACN)(S_2SiMe_2)$ (**2**)	1133/1123	63/64	520	29
$Co(O_2)(Tp^{Me2})(L^{Ph})$[b]	1150	60	543	21
$Co(O_2)(BDPP)$[c]	1135	65	n.r.	n.r.
$Co(O_2)(py)(salen)$[d]	1144	62	527	16
$Co(O_2)(Tp^{Me2})(CysOEt)$[e]	1152	61	n.r.	n.r.
$Co(O_2)(py)(TPP)$[f]	1143	60	520	19
$Co(O_2)(py)(tpfc)$[g]	1138/1094	63	547	11
$Co(O_2)(py)(Cl_8tpfc)$[g]	1146	61	509	21
$Co(O_2)(Hb)$[h]	1153/1122	57/56	537	23

[a] n.r.indicates not reported.

[b] Ref. 25.

[c] Ref. 22.

[d] Ref. 41.

[e] Ref. 28.

[f] Ref. 42.

[g] Ref. 43.

[h] Ref. 44.

Table 2.

Experimental and Calculated O-H BDFEs of Selected M(OOH) Complexes

Complex	Exp BDFE(O–H)	Calcd BDFE(O–H)
$Co(OO–H)(Me_3TACN)(S_2SiMe_2)$	66 – 70[a]	67
$Co^{III}(OO–H)(BDPP)$[b]	> 66[a]	69
$L^{Me}{}_2Cu^{II}{}_2(OO–H)$[c]	72[d]	—
$Fe^{III}(TMC)(SH)(OO–H)$[e]	—	70.3[f]
$[Fe^{III}(TMC)(NCH)(OO–H)]^+$[e]	—	75.4[f]
$[Fe^{II}(TMC)(OO–H)]^+$[g]	—	77.2[f]
$[(Me_6cyclam)Rh^{III}(HO)(OO–H)]^+$[h]	79.5[h]	—
$[(Me_6cyclam)Rh^{III}(H_2O)(OO–H)]^{2+}$[h]	80[h]	—
$[([14]aneN4)Co^{III}(HO)(OO–H)]^{2+}$[h]	80.9[h]	—
$[(H_2O)_5Cr^{III}OO–H]^{2+}$[h]	81.4[h]	—
$[(Me_6cyclam)Co^{III}(H_2O)(OO–H)]^{2+}$[h]	81.9[h]	—
H–OO–[h]	81.6[i]	—
HOO–H[h]	91[i]	—
*t*BuOO–H[h]	91.5[i]	—
$CH_3C(O)OO–H$[h]	95.1[i]	—

[a] estimated based on reported reactivity.

[b] ref22.

[c] ref 62.

[d] measured from E^0 and pK_a values in CH_3CN.

[e] ref 71.

[f] BDE, not BDFE, was calculated.

[g] ref 74.

[h] ref 67.

[i] measured from E^0 and pK_a values in H_2O.